Final Draft

of the original manuscript

Baranchikov, A.; Kopitsa, G.; Yorov, K.; Sipyagina, N.; Lermontov, S.; Pavlova, A.; Kottsov, S.; Garamus, V.; Ryukhtin, V.; Ivanov, V.:

SiO2–TiO2 Binary Aerogels: A Small-Angle Scattering Study.

In: Russian Journal of Inorganic Chemistry. Vol. 66 (2021) 6, 874 - 882.

First published online by Pleiades Publishing: 29.06.2021

https://dx.doi.org/10.1134/S003602362106005X

SiO_2–TiO_2 Binary Aerogels: A Small-Angle Scattering Study

A. E. Baranchikov[a, *], G. P. Kopitsa[b, c], Kh. E. Yorov[a], N. A. Sipyagina[d], S. A. Lermontov[d], A. A. Pavlova[b, e], S. Yu. Kottsov[a], V. M. Garamus[f], V. Ryukhtin[g], and V. K. Ivanov[a]

[a] *Kurnakov Institute of General and Inorganic Chemistry, Russian Academy of Sciences, Moscow, 119991 Russia*
[b] *St.-Petersburg Nuclear Physics Institute, National Research Center "Kurchatov Institute", Gatchina, 188300 Russia*
[c] *Grebenshchikov Institute of Silicate Chemistry, Russian Academy of Sciences, St.-Petersburg, 199034 Russia*
[d] *Institute of Physiologically Active Compounds, Russian Academy of Sciences, Chernogolovka, Moscow oblast, 142432 Russia* [e] *Saint Petersburg State University, St. Petersburg, 199034 Russia*
[f] *Helmholtz-Zentrum Hereon, Geesthacht, 21502 Germany*
[g] *Nuclear Physics Institute, ASCR, Řež, 25068 Czech Republic*
**e-mail: a.baranchikov@yandex.ru*

Abstract—Structural analysis in the range of characteristic sizes from 1 nm to ~1.5 μm was performed for SiO_2–TiO_2 aerogels prepared in supercritical CO_2, isopropanol, hexafluoroisopropanol, or methyl-*tert*-butylether using small-angle X-ray scattering and neutron scattering complementary methods. A two-level model that accounts for scattering by individual inhomogeneities and their aggregates, which have fractal properties, satisfactorily describes the aerogel structures over the entire range of scales. It is shown for the first time that the titania concentration is the key factor in the small-angle neutron and X-ray scattering by SiO_2–TiO_2 aero-gels. The phase composition of an aerogel does not significantly affect the aerogel structure in the range of scales from 1 nm to ~1.5 μm, as probed by small-angle X-ray and neutron scattering.

INTRODUCTION

Aerogels are a unique type of solid-phase materials distinguished by high specific surface areas and porosities, which make them useful in the design of structural materials, including heat and sound insulators [1]. Chemical modification of aerogels makes it possible to endow them with some functional properties important from a practical point of view for producing effective catalysts, selective sorbents, phosphors, and gas sensors [1–3].

In the context of application, of particular interest are multicomponent aerogels whose functional characteristics and textural properties can be set by their chemical composition, preparation and subsequent processing parameters [4–6]. SiO_2–TiO_2 binary aerogels are the best studied of these materials; they have high catalytic activities in some organic syntheses and have pronounced photocatalytic or UV protective properties [5, 7–12]. Importantly, the composition requirements for catalytic and photocatalytic SiO_2–TiO_2 materials differ significantly: high catalytic activity is provided by a high concentration of Si–O–Ti bonds, which is achieved in amorphous aerogels with high degrees of cross-polymerization of oxide components [13–15]. High photocatalytic activity, in contrast, is typical of materials that contain nanocrystalline titania, where Si–O–Ti bond concentration is relatively low [14–20].

To prepare SiO_2–TiO_2 binary aerogel materials one should keep in mind that the hydrolysis rates of silicon alkoxides and titanium alkoxides differ by orders of magnitude: e.g., for $Ti(OEt)_4$, the hydrolysis rate is five orders of magnitude higher than for $Si(OEt)_4$ (the rate constants are $k = 10^{-3}$ M^{-1} s^{-1} and $k = 5 \times 10^{-9}$ M^{-1} s^{-1}, respectively [21]). Therefore, coordination chemistry approaches will help to prepare high-porosity SiO_2–TiO_2 materials with reproducible properties. In particular, the use of organic ligands to chelate titanium atoms can significantly reduce the difference between the hydrolysis rates of titanium and silicon alkoxides and ensure the production of chemically homogeneous materials [22].

The most popular method for preparing aerogels is supercritical drying of the corresponding lyogels, with carbon dioxide or lower aliphatic alcohols usually used as supercritical fluids [1]. A supercritical fluid can react with the gel host, especially if the drying process occurs at a sufficiently high temperature [23–25]. Our experimental data indicate that the properties of the supercritical fluid used largely determine the compo-

sition and structure of the resulting aerogels [26]. However, the effect of this factor on the structure of aerogels has not yet been systematically analyzed over a wide range of scales.

We have previously studied the effect of the type of supercritical fluid (e.g., CO_2, isopropanol, hexafluoroisopropanol, and methyl-*tert*-butyl ether) on the physical and chemical properties (textural characteristics, phase composition, and thermal behavior) of SiO_2–TiO_2 aerogels with various titanium content (with the Ti : Si ratio ranging from 1 : 1 to 1 : 9 mol/mol) [27, 28]. Here, we continue this series of studies by a detailed analysis of the mesostructure of SiO_2–TiO_2 aerogels using small-angle X-ray scattering (SAXS) and ultra-small-angle neutron scattering (USANS).

EXPERIMENTAL

The details of synthesis of SiO_2 aerogels and SiO_2–TiO_2 binary aerogels can be found in our previous publications, together with the comprehensive analysis of physical and chemical properties of the prepared materials [26–28]. The synthesis of SiO_2–TiO_2 lyogels was carried out mixing pre-hydrolyzed tetramethoxysilane (TMOS), a solution containing titanium tetraisopropoxide (TIP) and acetylacetone (acacH), followed by addition of aqueous hydrogen fluoride solution as a gelation catalyst. SiO_2 lyogels were prepared by a similar procedure without titanium compounds added to the batch. Then, the lyogels were allowed to age at room temperature for 24 h, and washed with a solvent once a day during 5 days; the solvent was selected from isopropanol (*i*PrOH), methyl-*tert*-butyl ether (MTBE), and hexafluoroisopropanol (HFIP). The lyogels intended to be dried with supercritical CO_2 were washed with isopropanol.

The solvents used for supercritical drying were isopropanol, carbon dioxide, methyl-*tert*-butyl, and hexafluoroisopropanol. The details of supercritical drying procedure and the equipment used are described in our previous publications [26–28]. The drying temperatures and pressures were 255 ± 5°C and 6.5 ± 0.5 MPa for *i*PrOH, 240 ± 5°C and 6.5 ± 0.5 MPa for MTBE, 205 ± 5°C and 11 ± 1 MPa for HFIP, and 50 ± 1°C and 12 ± 0.2 MPa for CO_2. The critical parameters of the solvents used were: T_{cr} = 235°C and p_{cr} = 4.8 MPa for *i*-PrOH [29], T_{cr} = 224.1°C and p_{cr} = 3.4 MPa for MTBE [30, 31], T_{cr} = 182.0°C and p_{cr} = 3.1 MPa for HFIP [32], and T_{cr} = 31°C and p_{cr} = 7.4 MPa for CO_2 [29]. The supercritically dried aerogels were monolithic cylinders.

The SAXS structural analysis of aerogels was carried out on a P12 BioSAXS beamline [33] at the **Petra** III storage ring (at DESY, Hamburg) operating in point slit geometry. The setup was equipped with a Pilatus 2M (Dectris) gas-filled detector consisting of 172 × 172 μm^2 pixels with a total active area of 253.7 × 288.8 mm. The photon wavelength λ = 0.124 nm and the sample–detector distance L = 3 m allowed for scattered intensity measurements in the momentum transfer range 8×10^{-2} nm$^{-1} \le q \le 3$ nm^{-1}. Grounded aerogel samples were applied to a kapton film immediately prior to the experiment. Corrections were applied for scattering by the kapton film and ambient background. The thus-obtained 2D isotropic scattering patterns were azimuthally averaged with account for detector efficacy. All measurements were at room temperature. Primary data processing was in the ATSAS program package [34].

USANS measurements were carried out on a MAUD high-resolution double-crystal diffractometer (LVR-15 reactor, Prague) [35, 36]. A MAUD diffractometer, unlike ordinary double-crystal diffractometers, is equipped with an elastically bent Si-crystal analyzer, which can provide scattering intensity measurements by a one-dimensional position-sensitive detector over the entire available momentum transfer range without crystal rotation. Scattering intensities were measured in the momentum transfer range 4×10^{-3} nm$^{-1} < q < 2 \times 10^{-1}$ nm^{-1}. Prior to an experiment, powdery aerogel samples were poured into 1 mm quartz cells. The spectra were corrected for cell scattering, instrumental scattering, and ambient background using a routine procedure [36].

For getting opportunity of matching data gained by different methods, we stitched together the data gained by USANS (with collimation corrections for the two-crystal geometry) and SAXS in the momentum transfer range 8×10^{-2} nm$^{-1} \le q \le 2 \times 10^{-1}$ nm^{-1} (the range in which USANS and SAXS data overlap). So, the USANS and SAXS complementary methods gave us the full scattering pattern for SiO_2–TiO_2 aerogel samples with the momentum transfer range 4×10^{-3} nm$^{-1} < q < 3$ nm^{-1}, corresponding to the range of characteristic sizes (diameters) from 1 nm to ~1.5 μm.

RESULTS AND DISCUSSION

Figures 1a–1d show experimental USANS and SAXS $I_S(q)$ curves for titanium-free SiO_2 aerogel samples (Fig. 1a) and SiO_2–TiO_2 aerogels (Figs. 1b–1d) with various as-batch titania percentages (10, 20, and 50 mol %, respectively), which were prepared by supercritical drying in various supercritical solvents. A qualitative consideration of the data indicates that the major factor in the scattering character of aerogels is the titania concentration, so scattering curves for the aerogels with the same as-batch titania concentration synthesized using different supercritical fluids are similar.

This is rather nontrivial in view of our previous finding that the type of supercritical fluid used, which determines the supercritical drying temperature, has a

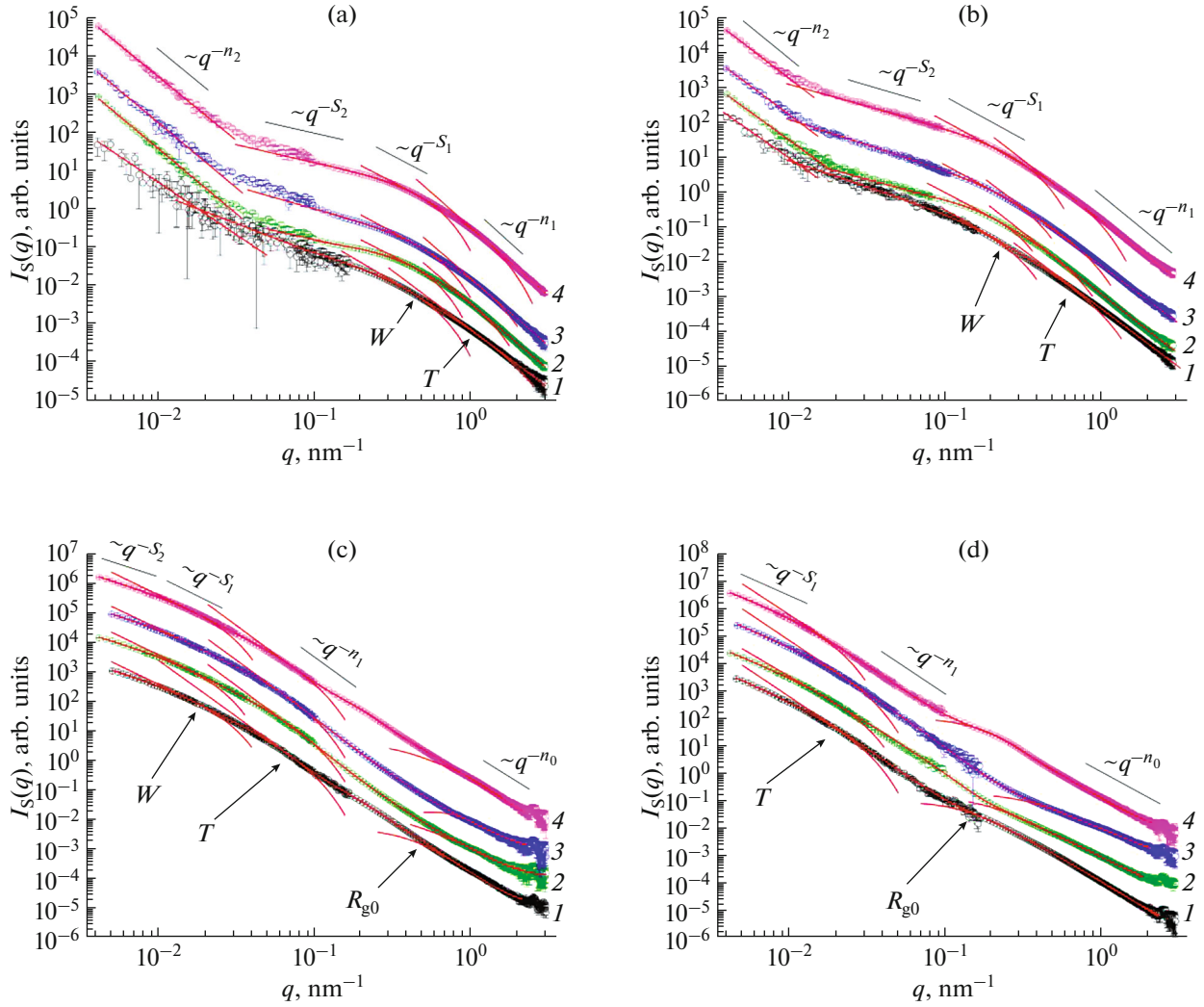

Fig. 1. $I_S(q)$, USANS and SAXS scattering intensity versus momentum transfer plots for (a) SiO_2, (b) SiO_2–TiO_2 (10 mol % TiO_2), (c) SiO_2–TiO_2 (20 mol % TiO_2), and (d) SiO_2–TiO_2 (50 mol % TiO_2) aerogels prepared by supercritical drying in (1) isopropanol, (2) CO_2, (3) hexafluoroisopropanol, and (4) methyl-*tert*-butyl ether. For clarity, the $I_S(q)$ for samples 2, 3, and 4 are multiplied by 10, 10^2, and 10^3, respectively. Arrows indicate data ranges corresponding to characteristic inhomogeneity sizes.

key effect on the phase composition SiO_2–TiO_2 aerogels [27, 28]. Supercritical drying in carbon dioxide or hexafluoroisopropanol yields X-ray amorphous aerogels, while supercritical drying in either isopropanol or methyl-*tert*-butyl yields aerogels containing nanocrystalline anatase with 10–20 nm particles [28]. At the same time, in contrast to diffraction methods, where X-ray or neutron scattering is due to the ordering of atoms in the sample structure, small-angle neutron and X-ray scattering is due to the contrast $\Delta\rho = \rho(r) - \rho_s$ (the difference between the mean scattering density of inhomogeneities $\rho(r)$ and the scattering density of the medium ρ_s), and the contrast is virtually independent of the short-range or long-range ordering in scattering inhomogeneities [37].

Figure 1a shows small-angle scattering intensity versus momentum transfer curves for titanium-free SiO_2 aerogel samples that were prepared by supercritical drying in various supercritical fluids. All curves feature two momentum transfer q ranges, where the scattering intensity $I_S(q)$ obeys the q^{-n} power law with different values of the exponent n_i. Such scattering is typical of two-level hierarchical structures [38], which are inherent to porous oxide materials with developed interfaces between phases (aerogels and xerogels) [39–44].

Scattering in the range of large momentum transfers ($q > 3 \times 10^{-2}$ nm^{-1}), corresponding to the smallest structural scale level, is typical of porous (solid–pore) systems consisting of randomly oriented nonspherical (anisometric) items, e.g., strongly elongated or flattened particles or pores. In order to describe scattering in the Guinier region, which is determined by the sizes and shapes of scattering inhomogeneities, one should use the generalized relationship [45]

$$\frac{d\sum(q)}{d\Omega} = \frac{G}{q^s}\exp\left(-\frac{q^2R_g^2}{3-s}\right), \quad (1)$$

where G is the Guinier factor [46], R_g is the radius of gyration of scattering inhomogeneities, s is a parameter determined by the inhomogeneity shape (for spherical items, $s = 0$, for one-dimensional particles or pores $s = 1$, and for two-dimensional inhomogeneities $s = 2$). Parameter s can acquire fractional values if scattering inhomogeneities are shaped as an ellipsoid, or if the system contains inhomogeneities of various shapes.

Since non-spherical items are defined not by one, but by two characteristic dimensions (radius R_c and length L in the case of elongated inhomogeneities) or three (thickness T, width W, and length L for flattened inhomogeneities), the Guinier region can comprise two or three momentum transfer q ranges, in full match with the experimental data (Fig. 1a).

Thus, three ranges can be distinguished on the scattering intensity versus momentum transfer curve for titanium-free SiO_2 aerogels, in the region of high momentum transfers ($q > 3 \times 10^{-2}$ nm^{-1}): a range corresponding to the local structure of scattering inhomogeneities, describable by the power function q^{-n_1} (the Porod law), and two scattering ranges where scattering is determined by the characteristic sizes and shapes of scattering inhomogeneities (Guinier law).

The values of exponent n_1 derived from the slopes of linear portions of experimental $I_S(q)$ plots at $q >$ 1 nm^{-1} fall in the range from 3.05 to 3.59. Thus, the first structural level of SiO_2 aerogels is represented by inhomogeneities having fractal interphase boundaries with fractal dimensions of $2.41 \le D_{S_1} = 6 - n_1 \le 2.95$ [47].

In view of the above, we turned to the generalized Guinier–Porod empirical model [45] to analyze scattering by SiO_2 aerogels at the first structural level (in the range $q > 3 \times 10^{-2}$ nm^{-1}),

$$\frac{d\sum(q)}{d\Omega} = \begin{cases} G_2\exp\left(-\dfrac{q^2R_{g_2}^2}{3}\right), & q < q_2 \\ \dfrac{G_1}{q^{s_1}}\exp\left(-\dfrac{q^2R_{g_1}^2}{3-s_1}\right), & q_2 < q < q_1, \\ \dfrac{B_1}{q^{n_1}}, & q_1 < q \end{cases} \quad (2)$$

where $(3 - s_1)$ is a dimensional factor, R_{g_1} and R_{g_2} are characteristic dimensions of non-spherical scattering inhomogeneities ($R_{g_1} < R_{g_2}$), G_2 and G_1 are Guinier factors [46], and B_1 is a factor of scattering inhomogeneity local structure [47]. $R_{g_2} = (L^2/12 + R^2/2)^{1/2}$ and $R_{g_1} = (R/2)^{1/2}$ for elongated inhomogeneities of radius R and length L; $R_{g_2} = (W^2/12 + T^2/12)^{1/2}$ and $R_{g_1} = (T/12)^{1/2}$ for flattened inhomogeneities of thickness T and width W.

Scattering in the range $q < 0.03$ nm^{-1}, detected by USANS and corresponding to the second structural level of a larger scale, is fitted by the power law q^{-n_2}. The values of n_2 for SiO_2 aerogels for which the hexafluoroisopropanol, methyl-*tert*-butyl ether, or CO_2 supercritical fluid was used, fall in the range from 3.33 to 3.41, indicating the surface fractal properties of second-level inhomogeneities, and $2.59 \le D_{S_2} = 6 - n_2 \le 2.67$. For an aerogel prepared with the isopropanol supercritical fluid, n_2 is 2.74, which corresponds to scattering on items with mass-fractal aggregation (the corresponding fractal dimension: $D_{M_2} = n_2 = 2.74$) [47]. This observation indicates a different aggregation character of inhomogeneities in the structure of this aerogel. Apparently, this is due to supercritical isopropanol drying being carried out at the highest temperature (255°C); under such conditions, the SiO_2 aerogel matrix can react with the solvent, this reaction is responsible for a partial structural reorganization of the aerogel.

The scattering intensity curves for all SiO_2 aerogels do not feature deviations from the power law in the $q <$ 3×10^{-2} nm^{-1} region and do not yield to the Guinier region. This circumstance indicates that the characteristic size of the second-level inhomogeneities exceeds the greatest size that can be determined by the setup used. However, the relationship $R_{max} \approx 3.5/q_{min}$ [48] could serve to estimate this size; the estimate was $R_{c_2} > 850$ nm.

So, the USANS data for SiO_2 aerogels in the small momentum transfer region ($q < 3 \times 10^{-2}$ nm^{-1}) was fitted by the power law

$$I_S(q) = \frac{B_2}{q^{n_2}}, \quad (3)$$

where B_2 is a factor depending on the local structure of second-level scattering inhomogeneities [47].

The results of fitting the small-angle X-ray and neutron scattering data $I_S(q)$ by relationships (2) and (3) for SiO_2 aerogels over the entire momentum transfer range appear in Table 1 and in Fig. 1a.

According to the fitting results, SiO_2 aerogels are highly porous systems comprised of flattened inhomogeneities with thickness T of 1.3 to 2.8 nm and width W of 7.9 to 10.8 nm, having developed fractal surfaces ($2.41 \le D_{S_1} \le 2.95$), in turn, constituting surface-fractal (or mass-fractal) aggregates with sizes $R_{c_2} > 850$ nm. The length L for first-level inhomogeneities cannot be estimated from the available data because of overlapping with scattering from second-level aggregates in the corresponding q range.

Table 1. Mesostructure parameters of SiO_2 aerogels prepared with various supercritical fluids, as derived from USANS and SAXS data using relationships (2) and (3)

Parameter	Supercritical fluid			
	*i*PrOH	CO_2	HFIP	MTBE
		USANS		
$D_{S_2} = 6 - n_2$	–	2.60 ± 0.03	2.59 ± 0.03	2.67 ± 0.03
$D_{M_2} = n_2$	2.74 ± 0.07	–	–	–
R_{c_2}, nm	> 850	> 850	> 850	> 850
		SAXS		
s_2	1.29 ± 0.02	0.57 ± 0.02	1.07 ± 0.02	0.85 ± 0.02
W, nm	8.1 ± 0.8	10.8 ± 0.9	7.9 ± 0.8	9.0 ± 0.9
s_1	2.38 ± 0.03	1.99 ± 0.02	2.13 ± 0.02	2.04 ± 0.02
T, nm	1.3 ± 0.1	2.8 ± 0.2	2.2 ± 0.2	2.4 ± 0.2
$D_{S_1} = 6 - n_1$	2.95 ± 0.03	2.52 ± 0.02	2.47 ± 0.02	2.41 ± 0.02

Using small-angle scattering methods to analyze the structure of highly porous materials, one should keep in mind that neutron and X-ray scattering occurs at interfaces between phases. Therefore, scattering inhomogeneities, whose sizes are derived from small-angle scattering data, can likewise be solid particles and pores in-between. In terms of commonly accepted models, the hydrolysis of silicon alkoxides and the condensation of colloidal SiO_2 particles should produce isotropic silica particles [49, 50], so it seems most reasonable that the scattering inhomogeneities constituting the first and second structural levels are pores between SiO_2 particles. Additionally, the sizes of first-level inhomogeneities are in satisfactory agreement with the pore distribution in identical SiO_2 aerogels as derived from low-temperature nitrogen adsorption data [27]. Similar considerations also apply to the interpretation of the results of structural analysis of mixed SiO_2–TiO_2 aerogels, which also consist of isotropic particles [51–53].

The SAXS character for SiO_2–TiO_2 aerogels with 10% titania as-batch concentration (Fig. 1b) is generally like that observed for titania-free SiO_2 aerogels (Fig. 1a). SAXS data also make it possible to recognize two momentum transfer q ranges where the scattering intensity $I_S(q)$ obeys the power law q^{-n}, with different exponents n_i. The comparison of Fig. 1a and Fig. 1b indicates that, when 10 mol % titania is added to aerogels, the segments of the intensity scattering curves that correspond to the Guinier mode for the first structural level and the power law segments ($q < 0.01$ nm^{-1}) for the second structural level shift toward the lower q. These shifts are likely due to slightly greater characteristic sizes of the first-level inhomogeneities in SiO_2–TiO_2 aerogels than in titania-free SiO_2 aerogels.

Scattering by SiO_2–TiO_2 (10 mol % TiO_2) aerogel samples was analyzed in terms of relationships (2) and (3). The results of data processing appear in Table 2 and in Fig. 1b.

An analysis of the contents of Table 2 shows that SiO_2–TiO_2 (10 mol % TiO_2) aerogels, like SiO_2 aerogels, consist of flattened primary inhomogeneities having fractal surfaces, which in turn constitute surface-fractal (or mass-fractal) aggregates. The structural differences between SiO_2–TiO_2 (10 mol % TiO_2) aerogels and SiO_2 aerogels are merely quantitative and due to the higher fractal surface dimensions of the second-level aggregates (for aerogels prepared with CO_2, HFIP, and MTBE supercritical fluids) and in the greater values of thickness T and width W of the first-level inhomogeneities. For SiO_2–TiO_2 (10 mol % TiO_2) aerogels, just as for SiO_2 aerogels, length L for first-level inhomogeneities cannot be estimated due to overlapping with scattering from second-level aggregates in the corresponding q range.

An increase in as-batch titania concentration in SiO_2–TiO_2 aerogels from 10 to 20 mol % leads to further changes in the observed scattering pattern (Fig. 1c), manifested in an additional shift, toward the lower q, of the segment where scattering from first-level inhomogeneities enters the Guinier mode. As a result of this shift, scattering from second-level aggregates in SiO_2–TiO_2 (20 mol % TiO_2) aerogels fitted by q^{-n_2} goes beyond the range detectable by the setup used. In this case, length L for first-level inhomogeneities cannot be determined, for it appreciably exceeds the greatest inhomogeneity size detectable by the instrument used. This is manifested as the absence of the third Guinier scattering range at small momentum transfer values with the dimensional factor $s_3 = 0$. Our estimate is that $L > 850$ nm in this case.

Table 2. Mesostructure parameters of SiO_2–TiO_2 (10 mol % TiO_2) aerogels prepared with various supercritical fluids, as derived from USANS and SAXS data using relationships (2) and (3)

Parameter	Supercritical fluid			
	*i*PrOH	CO_2	HFIP	MTBE
		USANS		
$D_{S_2} = 6 - n_2$	–	2.76 ± 0.05	2.76 ± 0.05	2.71 ± 0.05
$D_{M_2} = n_2$	2.72 ± 0.07	–	–	–
R_{c_2}, nm	> 850	> 850	> 850	> 850
		SAXS		
s_2	1.57 ± 0.03	0.89 ± 0.02	1.42 ± 0.02	1.01 ± 0.02
W, nm	14.5 ± 0.9	20.2 ± 1.2	13.3 ± 0.9	18.3 ± 1.0
s_1	2.65 ± 0.03	2.30 ± 0.02	2.37 ± 0.02	2.53 ± 0.02
T, nm	1.6 ± 0.2	4.3 ± 0.4	3.4 ± 0.3	2.4 ± 0.2
$D_{S_1} = 6 - n_1$	2.76 ± 0.03	2.47 ± 0.02	2.57 ± 0.02	2.51 ± 0.02

However, the scattering curves at high momentum transfer values ($q > 0.8$ nm^{-1}) feature an additional region where $I_S(q)$ is fitted by the power law q^{-n_0} with the exponent $n_0 = 3.33$ or 3.30 (for aerogels dried in *i*PrOH or MTBE, respectively) and 2.66 or 2.46 (for aerogels dried in CO_2 or HFIP, respectively). The appearance of this additional region is likely due to the presence of inhomogeneities with a prominent solid–solid interface in SiO_2–TiO_2 (20 mol %) aerogels. Such regions do not appear on the scattering curves for SiO_2–TiO_2 (10 mol %) aerogels, likely, due to the relatively low titania concentration in them. The characteristic size of such inhomogeneities in SiO_2–TiO_2 (20 mol %) aerogels was estimated at $R_{c_0} \approx 6$ nm. As we determined previously [27], SiO_2–TiO_2 (20 mol %) aerogels prepared via drying in supercritical *i*PrOH or MTBE contain nanocrystalline anatase particles sized ~15 nm (as determined by the Scherrer relationship). Thus, the match of diffraction data [27] and small-angle X-ray scattering data allows us to assume that the areas observed by SAXS in SiO_2–TiO_2 (20 mol %) aerogels dried in supercritical *i*PrOH or MTBE correspond to nanocrystalline anatase. Anatase particles in those aerogels as probed by SAXS have a fractal surface with the dimension $D_{S_0} = 6 - n_0 = 2.67$ and 2.70 (for *i*PrOH and MTBE, respectively). On the other hand, SiO_2–TiO_2 (20 mol %) aerogels dried in supercritical CO_2 or hexafluoroisopropanol are X-ray amorphous and contain no nanocrystalline anatase [27, 28]. Thus, the specified areas in these aerogels most likely correspond to local chemical inhomogeneity zones comprising primarily amorphous titania. In SiO_2–TiO_2 (20 mol %) aerogels dried in supercritical CO_2 or HFIP, such inhomogeneities have a mass-fractal type structure with the dimension $D_{M_0} = n_0 = 2.66$ and 2.46, respectively, as probed by SAXS.

Therefore, scattering in the $q > 0.8$ nm^{-1} range was fitted using a unified exponential-power relationship [48]

$$I_s(q) = G_0 \exp\left(-\frac{q^2 R_{g_0}^2}{3}\right) + B_0 \left[\frac{\left(\operatorname{erf}\left(\frac{qR_{g_0}}{\sqrt{6}}\right)\right)^3}{q}\right]^{n_0} + I_{inc}, \quad (4)$$

where G_0 is the Guinier factor, R_{g_0} is the radius of gyration of scattering inhomogeneities, B_0 is a factor depending on the local structure of scattering inhomogeneities, and constant I_{inc} describes background incoherent scattering by inhomogeneities of the order of X-ray wavelength. The R_{g_0} for fractal items is related to the upper self-similarity bound as $R_{c_0} = R_{g_0}\sqrt{(D_{S_0} + 2)/D_{S_0}}$ [54].

Norming the momentum transfer q to the error function erf(x) in expression (4) enables us to describe correctly scattering intensity in the gap between the area described by the Guinier approximation ($qR_{c_0} < 1$) and the area described by the power function q^{-n} ($qR_{c_0} \gg 1$), which is contributed by both inhomogeneities of characteristic scale R_{c_0}, and their surfaces [48].

Thus, the sum of relationships (2) and (4) was used to analyze scattering data for SiO_2–TiO_2 (20 mol % TiO_2) aerogels. The results of data processing appear in Table 3 and in Fig. 1c.

The comparison of the contents of Tables 2 and 3 shows that an increase in as-batch titania concentra-

Table 3. Mesostructure parameters of SiO_2–TiO_2 (20 mol % TiO_2) aerogels prepared with various supercritical fluids, as derived from USANS and SAXS data using relationships (2) and (4)

Parameter	Supercritical fluid			
	*i*PrOH	CO_2	HFIP	MTBE
		USANS		
s_2	1.70 ± 0.04	1.58 ± 0.03	1.73 ± 0.04	1.65 ± 0.02
W, nm	158 ± 8	189 ± 10	155 ± 8	166 ± 9
s_1	2.55 ± 0.02	2.54 ± 0.02	2.51 ± 0.01	2.55 ± 0.02
T, nm	27 ± 2	26 ± 2	28 ± 2	25 ± 2
$D_{S_1} = 6 - n_1$	2.21 ± 0.04	2.10 ± 0.04	2.15 ± 0.04	2.15 ± 0.04
		SAXS		
R_{c_0}, nm	5.7 ± 0.9	5.8 ± 0.8	6.2 ± 0.9	5.3 ± 0.8
$D_{S_0} = 6 - n_0$	2.67 ± 0.04	–	–	2.70 ± 0.04
$D_{M_0} = n_0$	–	2.66 ± 0.06	2.46 ± 0.06	–

Table 4. Mesostructure parameters of SiO_2–TiO_2 (50 mol % TiO_2) aerogels prepared with various supercritical fluids, as derived from USANS and SAXS data using relationships (2) and (4)

Parameter	Supercritical fluid			
	*i*PrOH	CO_2	HFIP	MTBE
		USANS		
s_1	2.54 ± 0.02	2.38 ± 0.02	2.46 ± 0.01	2.23 ± 0.02
T, nm	90 ± 10	108 ± 10	92 ± 10	169 ± 15
$D_{S_1} = 6 - n_1$	2.21 ± 0.04	2.22 ± 0.04	2.19 ± 0.04	2.18 ± 0.04
		SAXS		
R_{c_2}, nm	14.5 ± 1.8	11.6 ± 1.2	12.6 ± 1.5	13.3 ± 1.5
$D_{S_0} = 6 - n_0$	2.51 ± 0.04	–	–	2.60 ± 0.04
$D_{M_0} = n_0$	–	2.87 ± 0.03	2.45 ± 0.03	–

tion in SiO_2–TiO_2 aerogels from 10 to 20 mol % appreciably decreases the surface fractal dimension D_{S_1} of first-level inhomogeneities, i.e., leads to smoothing of their surfaces. In addition, their characteristic sizes (thickness T and width W) increase significantly (almost by one order of magnitude).

As the titania concentration in SiO_2–TiO_2 aerogels increases to 50%, their small-angle scattering character continues changing. For SiO_2–TiO_2 (50 mol % TiO_2) aerogels the scattering curves $I_S(q)$ feature only one linear segment (the Guinier mode), referring to first-level inhomogeneities. In addition, the scattering intensity curves also feature a region corresponding to scattering from the solid–solid interface, associated with nanocrystalline anatase particles or compositional inhomogeneities in the sample.

Scattering data for SiO_2–TiO_2 (50 mol % TiO_2) aerogels were analyzed by the sum of relationships (2) and (4). The results of data processing appear in Table 4 and in Fig. 1d.

The comparison of the contents of Tables 3 and 4 shows that the increase in titania concentration in SiO_2–TiO_2 aerogels from 20 to 50 mol % results in the increase both of the characteristic sizes (T) of the second-level inhomogeneities and of the size R_{c_0}, which corresponds to nanocrystalline anatase or chemically inhomogeneous areas. The estimates of R_{c_0} for SiO_2–TiO_2 (50 mol % TiO_2) aerogels prepared using *i*PrOH and MTBE supercritical fluids satisfactorily match the TiO_2 crystallite sizes derived by Scherrer relationship from X-ray diffraction data (14 and 19 nm, respectively) [27]. In addition, from Tables 1–4 it follows that the increasing titanium concentration in SiO_2–TiO_2 aerogels leads to a systematic increase in scattering inhomogeneity sizes. Our prior data [28] indicate that the increasing titanium concentration in SiO_2–

TiO_2 aerogels increases the mean pore size and thereby decreases the aerogel surface. Therefore, it looks most correct to regard the first-level and second-level scattering inhomogeneities in aerogels as characteristics of the pore space structure of the aerogels.

CONCLUSIONS

For the first time a comparative analysis of mesostructures of SiO_2–TiO_2 aerogels with titanium concentrations ranging from 0 to 50 mol % TiO_2, produced by supercritical drying with various supercritical fluids, namely, CO_2, isopropanol, methyl-*tert*-butyl ether, and hexafluoroisopropanol, was performed by means of small-angle neutron and X-ray scattering complementary methods. This allowed for the structural characteristics (characteristic sizes and fractal dimensions) of the aerogels over a wide range of scales from 1 nm to ~1.5 μm. A generalized two-level model, which accounts for scattering by individual inhomogeneities and their aggregates, appeared to give a satisfactory fit of aerogel structures over the entire range of scales. The key factor in the small-angle neutron and X-ray scattering character of the aerogel is the titania concentration, and not the type of supercritical fluid, the latter determining the phase composition of the aerogel. For SiO_2–TiO_2 aerogels with relatively high titanium concentrations (20 mol % TiO_2 or more), a match is observed between the inhomogeneity sizes determined from small-angle X-ray scattering data at high momentum transfers ($q > 0.8$ nm^{-1}), on the one hand, and the particle sizes of nanocrystalline titania derived by the Scherrer relationship from X-ray diffraction data, on the other.

ACKNOWLEDGMENTS

The studies were carried out using the equipment of the Center for Collective Use of the Kurnakov Institute of General and Inorganic Chemistry.

FUNDING

This work was supported by the Russian Science Foundation (grant no. 19-73-20125). The SAXS measurements were performed on CANAM (NPI CAS Řež) equipment supported by MŠMT project no. LM2015056.

CONFLICT OF INTEREST

The authors declare that they have no conflicts of interest.

REFERENCES

1. A. C. Pierre and G. M. Pajonk, Chem. Rev. **102**, 4243 (2002). https://doi.org/10.1021/cr0101306
2. A. Corma and H. Garcia, Adv. Synth. Catal. **348**, 1391 (2006). https://doi.org/10.1002/adsc.200606192
3. T. Shimizu, K. Kanamori, A. Maeno, et al., Chem. Mater. **28**, 6860 (2016). https://doi.org/10.1021/acs.chemmater.6b01936
4. J. E. Amonette and J. Matyas, Microporous Mesoporous Mater. **250**, 100 (2017). https://doi.org/10.1016/j.micromeso.2017.04.055
5. K. E. Yorov, I. V. Kolesnik, I. P. Romanova, et al., J. Supercrit. Fluids, **169**, 105099 (2020). https://doi.org/10.1016/j.supflu.2020.105099
6. M. A. Aegerter, N. Leventis, and M. M. Koebel, *Aerogels Handbook* (Springer, New York, 2011). https://doi.org/10.1007/978-1-4419-7589-8
7. B. Malinowska, J. Walendziewski, D. Robert, et al., Appl. Catal., B **46**, 441 (2003). https://doi.org/10.1016/S0926-3373(03)00273-X
8. M. Dusi, C. A. Müller, T. Mallat, et al., Chem. Commun. **2**, 197 (1999). https://doi.org/10.1039/a808374f
9. M. Beghi, P. Chiurlo, L. Costa, et al., J. Non-Cryst. Solids **145**, 175(1992). https://doi.org/10.1016/S0022-3093(05)80451-X
10. C. U. Ingemar Odenbrand, S. Lars, T. Andersson, et al., J. Catal. **125**, 541 (1990). https://doi.org/10.1016/0021-9517(90)90325-E
11. B. E. Yoldas, J. Non-Cryst. Solids **38–39**, 81 (1980). https://doi.org/10.1016/0022-3093(80)90398-1
12. A. B. Shishmakov, Y. V. Mikushina, O. V. Koryakova, et al., Russ. J. Inorg. Chem. **64**, 864 (2019). https://doi.org/10.1134/S0036023619070155
13. J. B. Miller, S. T. Johnston, and E. I. Ko, J. Catal. **150**, 311 (1994). https://doi.org/10.1006/jcat.1994.1349
14. D. C. M. Dutoit, M. Schneider, and A. Baiker, J. Catal. **153**, 16 (1995). https://doi.org/10.1006/jcat.1995.1118
15. D. C. M. Dutoit, M. Schneider, R. Hutter, et al., J. Catal. **161**, 651 (1996). https://doi.org/10.1006/jcat.1996.0227
16. A. A. Ismail and I. A. Ibrahim, Appl. Catal., A **346**, 200 (2008). https://doi.org/10.1016/j.apcata.2008.05.031
17. S. V. Ingale, P. B. Wagh, A. K. Tripathi, et al., J. Sol-Gel Sci. Technol. **58**, 682 (2011). https://doi.org/10.1007/s10971-011-2445-4
18. G. N. Shao, A. Hilonga, S. J. Jeon, et al., Powder Technol. **233**, 123 (2013). https://doi.org/10.1016/j.powtec.2012.08.025
19. M. Schneider and A. Baiker, Catal. Today **35**, 339 (1997). https://doi.org/10.1016/S0920-5861(96)00164-2
20. J. H. Lee, S. Y. Choi, C. E. Kim, et al., J. Mater. Sci. **32**, 3577 (1997). https://doi.org/10.1023/A:1018665910396
21. J. Livage, M. Henry, and C. Sanchez, Prog. Solid State Chem. **18**, 259 (1988). https://doi.org/10.1016/0079-6786(88)90005-2

22. D. A. Zherebtsov, S. A. Kulikovskikh, V. V. Viktorov, et al., Russ. J. Inorg. Chem. **64**, 165 (2019). https://doi.org/10.1134/S0036023619020220
23. F. Kirkbir, H. Murata, D. Meyers, et al., J. Non-Cryst. Solids **225**, 14 (1998). https://doi.org/10.1016/S0022-3093(98)00003-9
24. S. Yoda and S. Ohshima, J. Non-Cryst. Solids **248**, 224 (1999). https://doi.org/10.1016/S0022-3093(99)00250-1
25. S. A. Lermontov, E. A. Straumal, A. A. Mazilkin, et al., J. Phys. Chem. **120**, 3319 (2016). https://doi.org/10.1021/acs.jpcc.5b10461
26. S. Lermontov, A. Malkova, L. Yurkova, et al., J. Supercrit. Fluids **89**, 28 (2014). https://doi.org/10.1016/j.supflu.2014.02.011
27. K. E. Yorov, N. A. Sipyagina, A. N. Malkova, et al., Inorg. Mater. **52**, 163 (2016). https://doi.org/10.1134/S0020168516020035
28. K. E. Yorov, N. A. Sipyagina, A. E. Baranchikov, et al., Russ. J. Inorg. Chem. **61**, 1339 (2016). https://doi.org/10.1134/S0036023616110048
29. D. W. Matson and R. D. Smith, J. Am. Ceram. Soc. **72**, 871 (1989). https://doi.org/10.1111/j.1151-2916.1989.tb06237.x
30. V. Majer, V. Svoboda, and H. V. Kehiaian, *Enthalpies of Vaporization of Organic Compounds: A Critical Review and Data Compilation* (Oxford, 1985).
31. T. E. Daubert and G. Hutchison, AIChE Symp. Ser. **279**, 93 (1990).
32. T. Tsukahara, M. Harada, H. Tomiyasu, et al., J. Phys. Chem. A **112**, 9657 (2008). https://doi.org/10.1021/jp802508h
33. C. E. Blanchet, A. Spilotros, F. Schwemmer, et al., J. Appl. Crystallogr. **48**, 431 (2015). https://doi.org/10.1107/S160057671500254X
34. https://www.embl-hamburg.de/biosaxs/software.html.
35. P. Mikula, P. Lukáš, and F. Eichhorn, J. Appl. Crystallogr. **21**, 33 (1988). https://doi.org/10.1107/S0021889887008653
36. P. Strunz, J. Saroun, P. Mikula, et al., J. Appl. Crystallogr. **30**, 844 (1997). https://doi.org/10.1107/S0021889897001271
37. D. I. Svergun and L. A. Feigin, *X-ray and Neutron Small-Angle Scattering* (Nauka, Moscow, 1986) [in Russian].
38. G. Beaucage, T. A. Ulibarri, E. P. Black, et al., *Hybrid Organic-Inorganic Composites* (Washington, 1995). https://doi.org/10.1021/bk-1995-0585
39. S. A. Lermontov, G. P. Kopitsa, A. Y. Baranchikov, et al., J. Solid State Chem. **198**, 496 (2012). https://doi.org/10.1016/j.jssc.2012.11.022
40. V. K. Ivanov, G. P. Kopitsa, F. Y. Sharikov, et al., Phys. Rev. B: Condens. Matter Mater. Phys. **81**, 174201 (2010). https://doi.org/10.1103/PhysRevB.81.174201
41. G. P. Kopitsa, V. K. Ivanov, M. Sharp, et al., Russ. J. Inorg. Chem. **54**, 2091 (2009). https://doi.org/10.1134/s0036023609140022
42. S. V. Grigor'ev, V. M. Haramus, G. P. Kopitsa, et al., Russ. J. Inorg. Chem. **55**, 155 (2010). https://doi.org/10.1134/s0036023610020038
43. S. A. Lermontov, A. N. Malkova, N. A. Sipyagina, et al., Inorg. Mater. **53**, 1270 (2017). https://doi.org/10.1134/S002016851712007X
44. S. A. Lermontov, A. E. Baranchikov, N. A. Sipyagina, et al., Russ. J. Inorg. Chem. **65**, 255 (2020). https://doi.org/10.1134/S0036023620020084
45. B. Hammouda, J. Appl. Crystallogr. **43**, 716 (2010). https://doi.org/10.1107/S0021889810015773
46. A. Guinier and G. Fournet, *Small-Angle Scattering of X-rays* (John Wiley & Sons Inc., New York, 1955).
47. J. Teixeira, *Experimental Methods for Studying Fractal Aggregates* (Growth Form, Dordrecht, 1986). https://doi.org/10.1007/978-94-009-5165-5_9
48. G. Beaucage, J. Appl. Crystallogr. **28**, 717 (1995). https://doi.org/10.1107/S0021889895005292
49. A. C. Pierre and A. Rigacci, in *Aerogels Handbook* (Springer, New York, 2011). https://doi.org/10.1007/978-1-4419-7589-8_2
50. J. E. Elshof, R. Besselink, T. M. Stawski, et al., in *Sol-Gel Handbook* (Wiley-VCH Verlag GmbH & Co., Weinheim, 2015). https://doi.org/10.1002/9783527670819.ch21
51. E. Indrea, A. Peter, D. T. Silipas, et al., J. Phys. Conf. Ser. **182**, 012066 (2009). https://doi.org/10.1088/1742-6596/182/1/012066
52. V. Torma, H. Peterlik, U. Bauer, et al., Chem. Mater. **17**, 3146 (2005). https://doi.org/10.1021/cm047996n
53. W. Sari, D. Fitriyani, E. G. R. Putra, et al., AIP Conf. Proc. **1202**, 185 (2010). https://doi.org/10.1063/1.3295595
54. C. Oh and C. M. Sorensen, J. Colloid Interface Sci. **193**, 17 (1997). https://doi.org/10.1006/jcis.1997.5046

Translated by O. Fedorova